Inorganic Chemistry

pubs.acs.org/IC Article

Manganese Defective Clustering: Influence on the Spectroscopic Features of Ceria-Based Nanomaterials

D. C. Amaral, L. S. R. Rocha, L. I. Granone, M. M. Lage, M. S. Churio, M. D. Sanchez, E. Longo, H. M. S. Nascimento, M. Assis,* F. Moura, and M. A. Ponce

Cite This: *Inorg. Chem.* 2023, 62, 12392−12402 Read Online

ACCESS | Metrics & More | Article Recommendations | Supporting Information

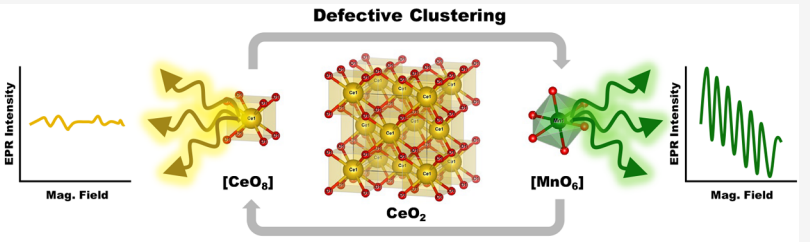

ABSTRACT: The influence of manganese modification on the spectroscopic features of manganese-doped CeO_2 systems synthesized by the microwave-assisted hydrothermal route and their correlation with the presence of O defective structures were verified, focusing on their interaction with poisonous atmospheres. Raman and electron paramagnetic resonance studies confirmed the presence of defective clusters formed by dipoles and/or quadrupoles. The number of paramagnetic species was found to be inversely proportional to the doping concentration, resulting in an increase in the Mn^{2+} signal, likely due to the reduction of Mn^{3+} species after the interaction with CO. X-ray photoelectron spectroscopy data showed the pure system with 33% of its cerium species in the Ce^{3+} configuration, with an abrupt decrease to 19%, after the first modification with Mn, suggesting that 14% of the Ce^{3+} species are donating one electron to the Mn^{2+} ions, thus becoming nonparamagnetic Ce^{4+} species. On the contrary, 58% of the manganese species remain in the Mn^{2+} configuration with five unpaired electrons, corroborating the paramagnetic feature of the samples seen in the electron paramagnetic resonance study.

1. INTRODUCTION

The cerium electron configuration (Xe) $6s^2\ 4f^2\ 5d^0$ generates two stable valence states, Ce^{3+} and Ce^{4+}, owing to the exchange interaction phenomenon, experimentally proven by magnetic and Mössbauer studies,[1] in which the individual magnetic moments of dipoles attempt to align themselves with all other magnetic moments within the material. It is worth mentioning that because of Hund's rule and the exchange interaction energy, the element cerium exhibits an unpaired electron in the 4f orbital, giving rise to its paramagnetic feature, which is unaffected by pressures of ≤50 GPa, as reported by Lipp et al.[2] This exchange interaction takes into account conduction−electron spin polarization effects and charge fluctuation contributions, which are fundamental for systems in which the localized levels approach the Fermi energy.[3] Additionally, it was shown that ceria-based magnetic susceptibilities also depend on crystal field effects.[4]

Cerium dioxide (CeO_2), or ceria, is one of the most studied Ce-based oxides in the literature, being widely applied as a catalyst, gas sensor, optical material, biomaterial, etc.[5] The structure of CeO_2 can spontaneously promote the appearance of defects such as isolated cationic O vacancies and vacancy complexes $[CeO_7{\cdot}V_o^{i}]$ (where i can be 0, +1, or +2, represented in the Kröger−Vink notation as $[CeO_7{\cdot}V_o^{x}]$, $[CeO_7{\cdot}V_o^{\bullet}]$, or $[CeO_7{\cdot}V_o^{\bullet\bullet}]$, respectively), also known as vacancy clusters. These agglomerates are intricately linked to the properties of CeO_2 and, consequently, its performance in a given application. In particular, in addition to its charge, the $[CeO_7{\cdot}V_o^{\bullet}]$ cluster has magnetic properties and, according to the literature, is formed preferentially.[6−8] In addition, the ability to release or absorb oxygen during the redox process, known as oxygen storage capacity (OSC), allows its use as both an active catalyst in a wide variety of catalytic reactions[9−11] and an essential component for the development of gas sensors aimed at environmental air monitoring. In this context, the search and development of new materials and technologies for this field of application arise from the growing need for efficient and environmentally friendly energy sources, not to mention the strict control of atmospheric air quality in industries and household appliances.[12,13]

Received: May 16, 2023
Published: July 21, 2023

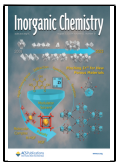

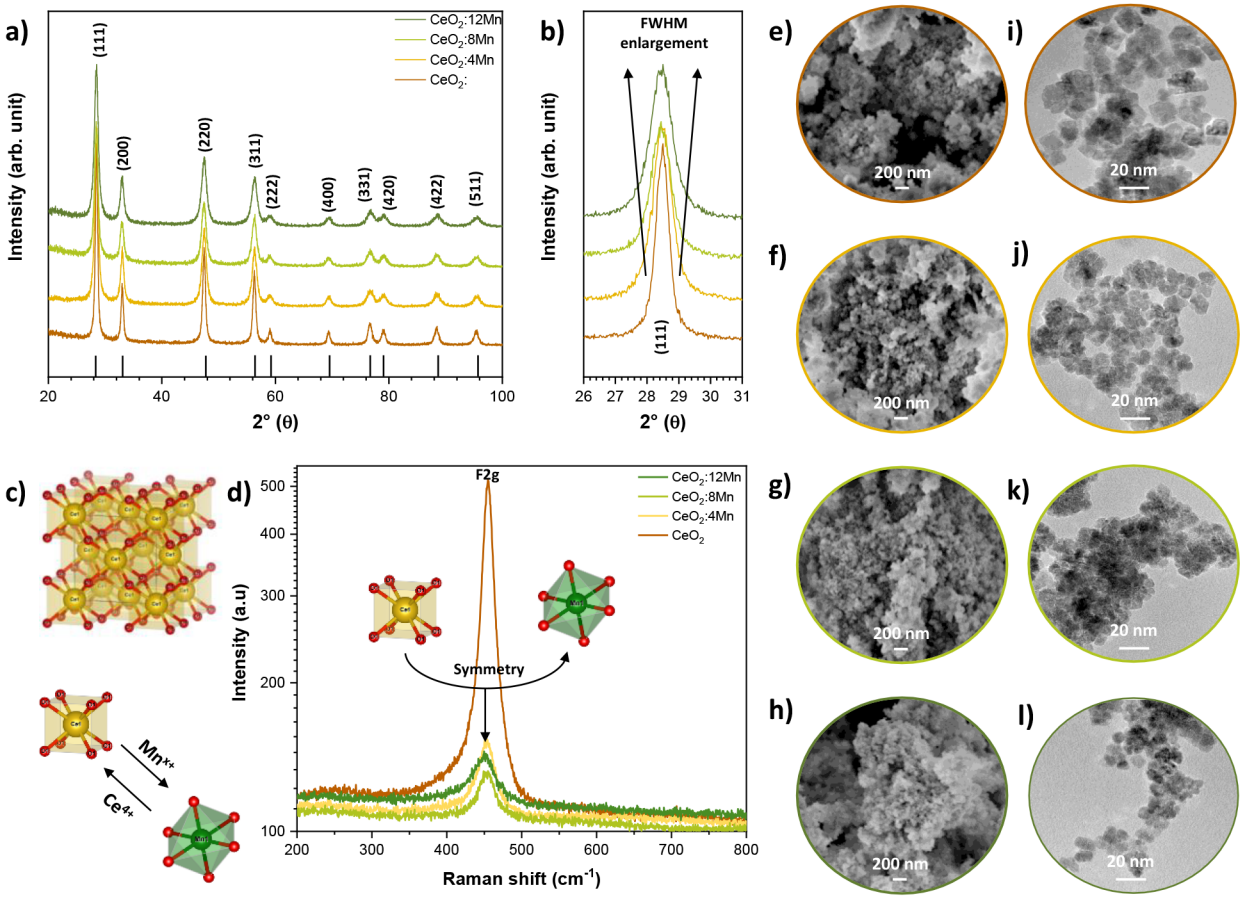

Figure 1. (a) XRD spectra for the pure and Mn-doped samples. (b) Detailed analysis of the (111) plane. (c) Crystalline structure of CeO_2. (d) Raman spectroscopy. (e–h) FEG-SEM of the pure and doped powders after calcination at 500 °C. (i–l) TEM images of the pure and doped samples.

One way to control and modulate defects, especially vacancy clusters, is the substitution or doping of transition metals in the CeO_2 structure. This can lead to the formation of defects in the forbidden region of the band gap of CeO_2, causing the promotion of electrons to the 4f states of Ce, which are responsible for determining the properties of this semiconductor.[14,15] The introduction of elements with different oxidation states or ionic radii into the CeO_2 sublattice, e.g., Ca^{2+}, Mg^{2+}, and Gd^{3+}, has already proven to be effective in improving the properties of this semiconductor.[16−18] Due to its electronic properties, manganese (Mn) is a dopant that has been extensively used to change the properties of semiconductors, in particular their electronic, optical, and structural properties.[19] Mn can exhibit multivalent oxidation states when MnO_y−CeO_x solid solutions are formed. In addition to Mn^{2+}, both Mn^{3+} and Mn^{4+} ions can enter the CeO_x structure according to several reports.[20−24]

Bearing this in mind, in this work, we sought to promote the creation of defective clusters in the material lattice by doping it with Mn, reinforcing the n-type behavior as a consequence of the creation of O vacancies and vacancy complexes. For this purpose, we synthesized pure and Mn-doped CeO_2 systems (4, 8, and 12 wt % Mn) by the microwave-assisted hydrothermal (MAH) route followed by calcination at 500 °C. Applied characterizations by X-ray diffraction (XRD), Raman spectroscopy, field emission gun scanning electron microscopy (FE-SEM), transmission electron microscopy (TEM), electron paramagnetic resonance (EPR) spectroscopy, and X-ray photoelectron spectroscopy (XPS) were used to investigate the influence of Mn modification on the presence of defective structures, which were specifically examined and correlated with the multifunctionality of this element, with a particular interest in the detection of CO atmospheres.

2. EXPERIMENTAL PROCEDURES

Pure and Mn-doped CeO_2 ($Ce_{1-0.5x}Mn_xO_2$ for x = 0, 4, 8, and 12 wt % Mn) particles were prepared using the MAH route. First, cerium nitrate hexahydrate [$Ce(NO_3)_3{\cdot}6H_2O$, NEON, 99%] and manganese nitrate tetrahydrate [$Mn(NO_3)_2{\cdot}4H_2O$, CRQ, analytical grade] salts were dissolved in distilled water while being stirred and heated at 60 °C. Subsequently, the nitrate solution was poured into the cerium solution followed by adjustment of the pH to 10. The solution was allowed to continue to stir for 40 min for complete homogenization and transferred to a Teflon vessel, which was then inserted into the microwave equipment (2.45 GHz, 800 W). The obtained solutions were irradiated to 100 °C at a heating rate of 10 °C/min and kept at this temperature for 8 min. Afterward, the solutions were cooled to room temperature and centrifuged at 2000 rpm for 45 min three times followed by a drying process in a laboratory oven at 100 °C for 48 h. Postsynthesis calcination of the powders was carried out in atmospheric air at 500 °C for 2 h at a heating rate of 10 °C/min.

XRD analysis was performed using a D/Max-2500PC diffractometer (Rigaku) with Cu Kα radiation (λ = 1.5406 Å). Raman spectroscopy was carried out on an iHR550 spectrometer (Horiba Jobin-Yvon) with a charge-coupled device detector and an argon-ion laser (MellesGriot) operating at 633 nm and a power of 200 mW. The

https://doi.org/10.1021/acs.inorgchem.3c01597
Inorg. Chem. 2023, 62, 12392−12402

morphologies and textures of the samples were observed using a Supra 35VP field emission scanning electron microscope operating at 10 kV (Carl Zeiss), as well as with high-resolution transmission electron microscopy (HR-TEM) using an FEI Tecnai G2-20 instrument (200 kV). EPR experiments were carried out at room temperature before and after CO(g) exposure (800 ppm at a pressure of 760 mmHg for 24 h) on an ELEXSYS E500T spectrometer (Bruker) equipped with an ER 4102ST rectangular resonator operating in the TE102 mode at a frequency of 9.8 GHz (X-band). The following data acquisition parameters were used for the measurements: a modulation frequency of 100.00 kHz, a modulation amplitude of 0.10 mT, a microwave power of 3.22 mW, a central field of 344.5 mT, a sweep width of 125 mT, and a time constant of 20.48 ms. A total of 1024 data points were collected per scan, and the resulting spectra were the average of 20 scans. For quantitative analyses, the total signal intensity was determined by calculating the area below the curve corresponding to the first integral of the EPR spectrum. The measured intensities were standardized according to the masses of the samples. The simulation of the EPR spectra was carried out using WinSim 2002 software (NIEHS). XPS was performed on an ESCA PHI 548 spectrometer with Mg Kα nonmonochromatic radiation at 250 W and 20 mA. The resolution spectra were recorded at a pass energy of 50 eV and a base pressure of $>5 \times 10^{-10}$ Torr. An electron flood gun was used for charge compensation, and the energy scale was calibrated on the basis of the high-binding energy side peak of the ceria 3d region at 916.7 V. Signal deconvolution was performed using Shirley-type background subtraction and an asymmetric sum of Gaussian−Lorentzian functions. The obtained binding energies were determined with an absolute resolution of 0.5 eV. Because Ce is the dominant element, all spectra were normalized by the maximum intensity of the peak centered at 916.7 eV after background subtraction, favoring comparisons between them.

3. RESULTS AND DISCUSSION

XRD analyses were performed to verify the order and disorder parameters along the range and to analyze the phase and purity of the synthesized samples. Figure 1a shows the diffractograms obtained for pure and Mn-doped CeO_2 samples. All samples were identified as CeO_2 with a fluorite-type cubic phase and space group $Fm\bar{3}m$, according to the Inorganic Crystal Structure Database (ICSD), pattern 24887. No secondary phases can be observed, evidencing the high purity of the samples obtained. A more detailed analysis of the most intense diffraction peak in the (111) direction is depicted in Figure 1b. As verified, the addition of Mn^{2+} to the structure results in a broadening, demonstrating that doping with Mn^{2+} increases the degree of long-distance disorder of the CeO_2 structure. To corroborate this result, the full width at half-maximum (fwhm) of this peak was calculated, ranging from 0.45° for the pure CeO_2 sample to 0.65°, 0.66°, and 0.74° for the CeO_2:4Mn, CeO_2:8Mn, and CeO_2:12Mn samples, respectively. From these values, we estimated the average crystallite sizes (d) using the Debye−Scherrer method. The d values were 19.0, 13.2, 13.0, and 11.6 nm, from the pure sample to the most doped sample, respectively.

The CeO_2 structure is theoretically formed by slightly distorted cubic [CeO_8] clusters with each vertex containing one O atom (Figure 1c). Such changes can be explained by the distorted octahedral [MnO_6] clusters that may be created within the CeO_2 structure, which alter the periodicity of the crystalline system.

Raman spectroscopy was used to evaluate the short-range order symmetry of the samples and corroborate the formation of defective clusters and structural defects. The results for the pure and Mn-doped samples are shown in Figure 1d. A clear peak around 450 cm^{-1} can be observed in all samples, depicting the primary F_{2g} mode, which is associated with the symmetrical stretching/breathing mode of O atoms around Ce cations.[25] As one can see, the pure CeO_2 samples have higher intensity in this mode, and the lack of any other mode indicates a highly symmetric system in both short- and long-range orders. This mode is very sensitive to any disturbance of the oxygen sublattice,[26] verified by the clear decrease in its intensity when the system started to be doped.[27]

This reduction can be linked to the formation of Mn [MnO_6] clusters, which replace the ceria [CeO_8] ones. These clusters have a lower electron density, owing to the presence of oxygen vacancies and their consequent nonresonant scattering of tunneling electrons.[28] Moreover, an increase in the number of electrons in the excited state is expected due to the Ce $4f^1$ orbital, leading to variations in the electrical properties of the semiconductor resulting from the hopping of electrons,[28] in addition to their fundamental role in the interaction with adsorbed oxygen and water molecules located on the crystal surface.[29,30]

The crystallite sizes of the CeO_2 samples can be estimated from the Raman line broadening (fwhm) with the simple equation reported by Phokha et al.[31] and Kosacki et al.,[32] based on the study by Weber, Hass, and McBride,[33] using a Lorentzian line shape for the fwhm estimate. It is worth mentioning that this approach can be generalized for quantitative nanoscale Raman spectroscopy.[34] According to the results, the fwhm value increases as the amount of Mn also increases in the CeO_2 crystalline lattice (19.2, 25.5, 25.7, and 35.5 cm^{-1} for CeO_2, CeO_2:4Mn, CeO_2:8Mn, and CeO_2:12Mn, respectively). This increase can be interpreted as a significant enhancement of phonon−phonon scattering,[35] which could be indicative of the creation of local distortions such as oxygen vacancies and their complexes. The estimated crystallite sizes were found to be 13.6, 8.0, 7.9, and 4.9 nm from the lowest to the highest Mn content, respectively. It is worth mentioning that these values are close to those obtained from the XRD measurements, following the same general downward trend with an increase in Mn doping.

At this point, it is worth mentioning that Scherrer derived his equation for the ideal condition of a perfectly parallel, infinitely narrow, and monochromatic X-ray beam incident on a monodisperse powder of cube-shaped crystallites. In addition, it is important to note that Scherrer's equation can be applied only for average sizes up to approximately 100−200 nm (depending on the instrument, sample, and signal-to-noise ratio) because diffraction-peak broadening decreases with an increase in crystallite size and it becomes difficult to separate the peak broadening due to crystallite size from the broadening due to other factors.[36] Therefore, the slight differences between the two methods can be ascribed to the use of Lorentzian and Gaussian line shapes for the fwhm estimation and the distinct proportionality constants that can be used.[33]

Indeed, according to Yang and Zhang,[37] the increase in the fwhm of the F_{2g} mode as a function of Mn^{2+} is due to the higher number of oxygen vacancies in CeO_2. In this sense, Conceição et al.[38] observed a gradual increase in the defect concentration by increasing the Gd content in ceria, with the charge balance being kept through the formation of oxygen vacancies with distinct charges depending on the amount of Gd.

As observed in the FE-SEM images (Figures 1e−h) of the pure and Mn-doped CeO_2 samples, there is no well-defined

https://doi.org/10.1021/acs.inorgchem.3c01597
Inorg. Chem. 2023, 62, 12392−12402

morphology, even after calcination at 500 °C. The average size of the particles was calculated to be 30−40 nm, with a high degree of agglomeration, likely due to electrostatics and van der Waals forces.[39] Indeed, from the HR-TEM observations (Figures 1i−l), the particles showed average sizes close to 20 nm, which corroborates their agglomeration and the formation of clusters seen in the FEG-SEM images up to 40 nm. Zhou et al.[40] were able to obtain CeO_2 nanoparticles (NPs) with cubic morphologies by the hydrothermal method using $Na_3PO_4 \cdot 12H_2O$ as a surfactant, but at a synthesis temperature of 200 °C and a synthesis time of 20 h after calcination at 500 °C for 4 h. In this sense, the microwave-assisted hydrothermal route was found to be more advantageous for the preparation of ceria-based NPs because of the reduced costs of the synthesis procedure. On the basis of the analysis by Chen and Chen,[41] Mn doping tends to enhance grain boundary mobility due to the large distortion of the surrounding lattice, facilitating the migration of defects from the matrix (i.e., CeO_2), an ionic radius value that is much smaller than that of Ce^{4+}, and the relaxation of strain induced by the substitution of Ce^{4+} with ions with smaller radii.[42] Therefore, the nanometric behavior of the particles can be perceived with an overall reduction of their sizes with an increase in Mn content, which in turn inhibits grain growth due to the reduced number of effective shocks by the action of $[MnO_4]$ clusters with a lower electron density. On the contrary, the replacement of $[CeO_6]$ by $[MnO_6]$ clusters increases the concentration of oxygen vacancies, inducing relaxation in the crystalline lattice.

Figure 2 shows the EPR spectroscopy images for the samples before and after treatment with CO. This treatment was performed to analyze the potential of the samples to oxidize CO through a saturation of the material with CO in an atmosphere containing 760 mmHg of 800 ppm CO for 24 h at 400 °C (which is the temperature that guarantees an oxidation reaction without affecting the crystalline structure of CeO_2).[43] The Mn-doped samples before the CO treatment (Figure 2a) exhibit intense signals, which can be described as the convolution of two overlapping sextets and a broad Lorentzian curve. Both sextets, with g values of 1.999 and 1.998 and average hyperfine coupling constants A of 103.8 and 100.0 G, respectively, can be ascribed to the characteristic $|-^1/_2, m_I\rangle \leftrightarrow |+^1/_2, m_I\rangle$ transitions of Mn^{2+} centers.[44] As one can see, the integrated intensity of the total spectrum increases as a function of the amount of Mn, but not linearly. Although the Mn^{2+}, Mn^{3+}, and Mn^{4+} ions can enter the CeO_2 crystalline lattice,[45] the Mn^{3+} ions exhibit a large zero-field splitting, therefore being EPR-silent at conventional X-band frequencies.[46,47] A sextet with an EPR signal similar to that of Mn^{2+} but with a lower hyperfine constant A (76 G) can be attributed to the presence of Mn^{4+}.[48] Such a signal is either absent or hidden by the intense signal of Mn^{2+} ions. A broad singular line with a g value of 1.94 similar to the Lorentzian curve shown in Figure 2b was reported as being typical of Mn^{4+} in MnO_2 samples due to dipole−dipole and exchange interactions between these ions.[49] In addition, a similar signal was described as being the result of ligand field fluctuations and spin−spin interactions in highly concentrated Mn^{2+} samples.[50]

The analysis of the relative contributions from the simulation procedure (such as that shown in Figure 2b) indicates that the broad single line accounts for ∼84% of the total EPR spectra for the samples not treated with CO. On this basis, Mn^{4+} cannot be discarded as one of the species contributing to the broad singlet component of the EPR spectrum, in agreement with the DFT+U calculations reported by García Pintos et al.[44] The formation of further oxygen vacancies results in the reduction from Mn^{4+} to Mn^{3+} and from Mn^{3+} to Mn^{2+}. Therefore, in highly defective structures such as those reported herein, the oxidation states of Mn are mainly +3 and +2, although Mn^{4+} may also be present.

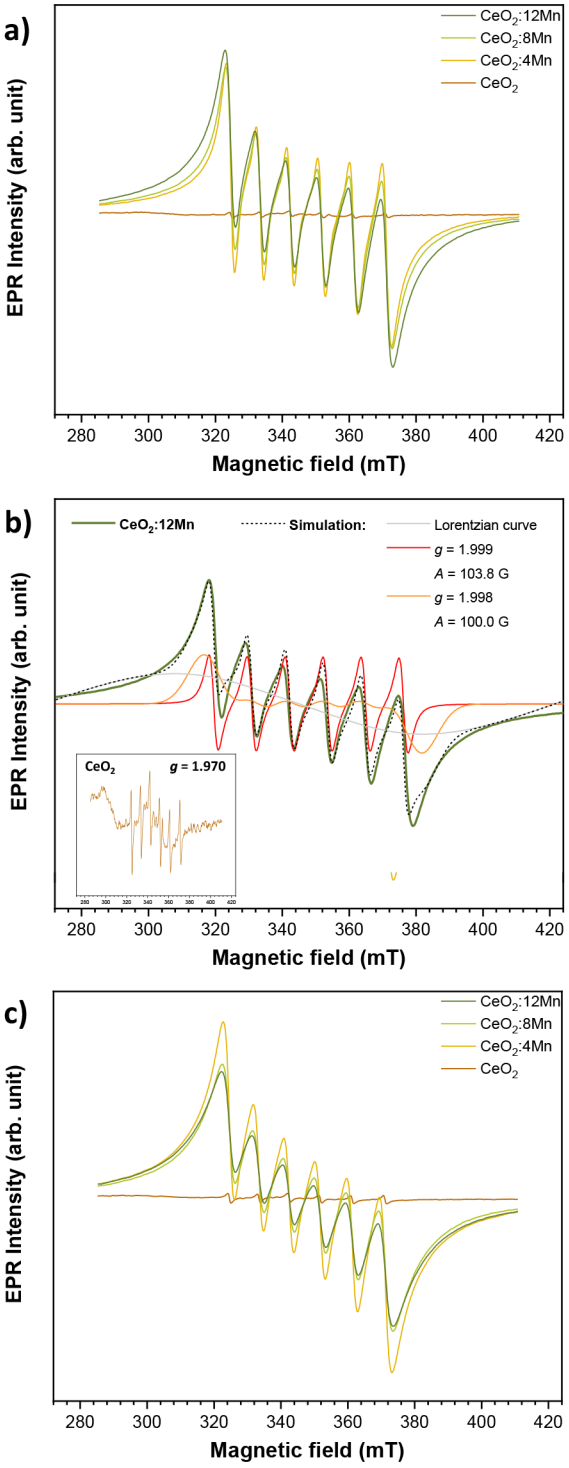

Figure 2. (a) EPR spectroscopy images for the samples before treatment with CO. (b) Analysis of the relative contributions from the simulation procedure in comparison to the sample doped with 12 wt % Mn. (c) Spectra after treatment with CO.

https://doi.org/10.1021/acs.inorgchem.3c01597
Inorg. Chem. 2023, 62, 12392−12402

Figure 3. (a) Formation of clusters in pure ceria. (b) Formation of clusters after the first introduction of Mn^{2+}. (C) Formation of clusters for >4 wt % Mn.

After treatment with CO (Figure 2c), an increase in the intensity of the EPR signals is observed for all samples. The increase in the Mn^{2+} signal corresponds to the reduced number of oxidized species of manganese with an oxidation state of greater than +2. One can then conclude that Mn not only is present in the +2 oxidation state but also is in equilibrium with other higher oxidation states. Thus, manganese species must be previously oxidized during their substitution in the lattice (i.e., Mn^{3+} and Mn^{4+}).

Valuable information concerning the oxidation state of Ce in CeO_2 samples can also be accessed by EPR spectroscopy. A line with a g value of 1.97 typically observed in CeO_2 samples is ascribed to electrons trapped near the surface of Ce^{4+}/Ce^{3+} redox pairs.[51] Even though this signal is present in the undoped sample (inset of Figure 2c), as the Mn content in the samples increases, this weak $g \sim 1.97$ line becomes negligible compared to that of the intense Mn^{2+} signals. Therefore, it is unfeasible to analyze the evolution of the signal of trapped electrons near the surface of Ce^{4+}/Ce^{3+} redox pairs with an increase in Mn concentration.

The formation of clusters of pure ceria is represented in Figure 3a. The scheme proposes the possibilities of interaction between the clusters that generate neutral systems as well as dipoles and quadrupoles.[52−54] As already mentioned, such an oxidized configuration is a consequence of the presence of a high concentration of O defects in the MnO_y−CeO_x solid solutions.[45] On the contrary, Ce^{3+} and Mn^{2+} cations are also responsible for reducing the vacancies from $V_o^{\bullet}$ to V_o^{x} or $V_o^{\bullet\bullet}$ to V_o^{x}, as illustrated in Figure 3b.

First, the balance between the resonant octahedral ordered (o) and disordered (d) clusters is represented by entity (i), in which the $[CeO_6]^x$ clusters account for the Ce^{4+} species (Figure 3a). Another point that must be taken into account is the intrinsic generation of oxygen vacancies and more complex defective clusters (ii), a process that gives rise to a $[CeO_6]'$ cluster, representing Ce^{3+}, and a singly ionized oxygen vacancy $[V_o^{\bullet}]$. These $[CeO_6]'$ clusters can act as electron donors, whereas the $[CeO_6]^x$ clusters can act as electron acceptors. Singly ionized oxygen vacancies, on the contrary, can act as both electron donors and acceptors. Therefore, the electronic exchange between a singly ionized oxygen vacancy $[V_o^{\bullet}]$ and a $[CeO_6]^x$ cluster results in the formation of a doubly ionized oxygen vacancy $[V_o^{\bullet\bullet}]$ and an additional $[CeO_6]'$ cluster (iii), thus decreasing the Ce^{4+}/Ce^{3+} ratio. In contrast, the electronic exchange between a $[CeO_6]'$ cluster and a singly ionized oxygen vacancy $[V_o^{\bullet}]$ generates a neutral oxygen vacancy $[V_o^{x}]$ and a $[CeO_6]^x$ cluster (iv), thus increasing the Ce^{4+}/Ce^{3+} ratio. It is worth mentioning that the Ce^{3+} species are located preferentially close to the oxygen vacancies.[55−57] The mechanism presented above for the formation of neutral

https://doi.org/10.1021/acs.inorgchem.3c01597
Inorg. Chem. 2023, 62, 12392−12402

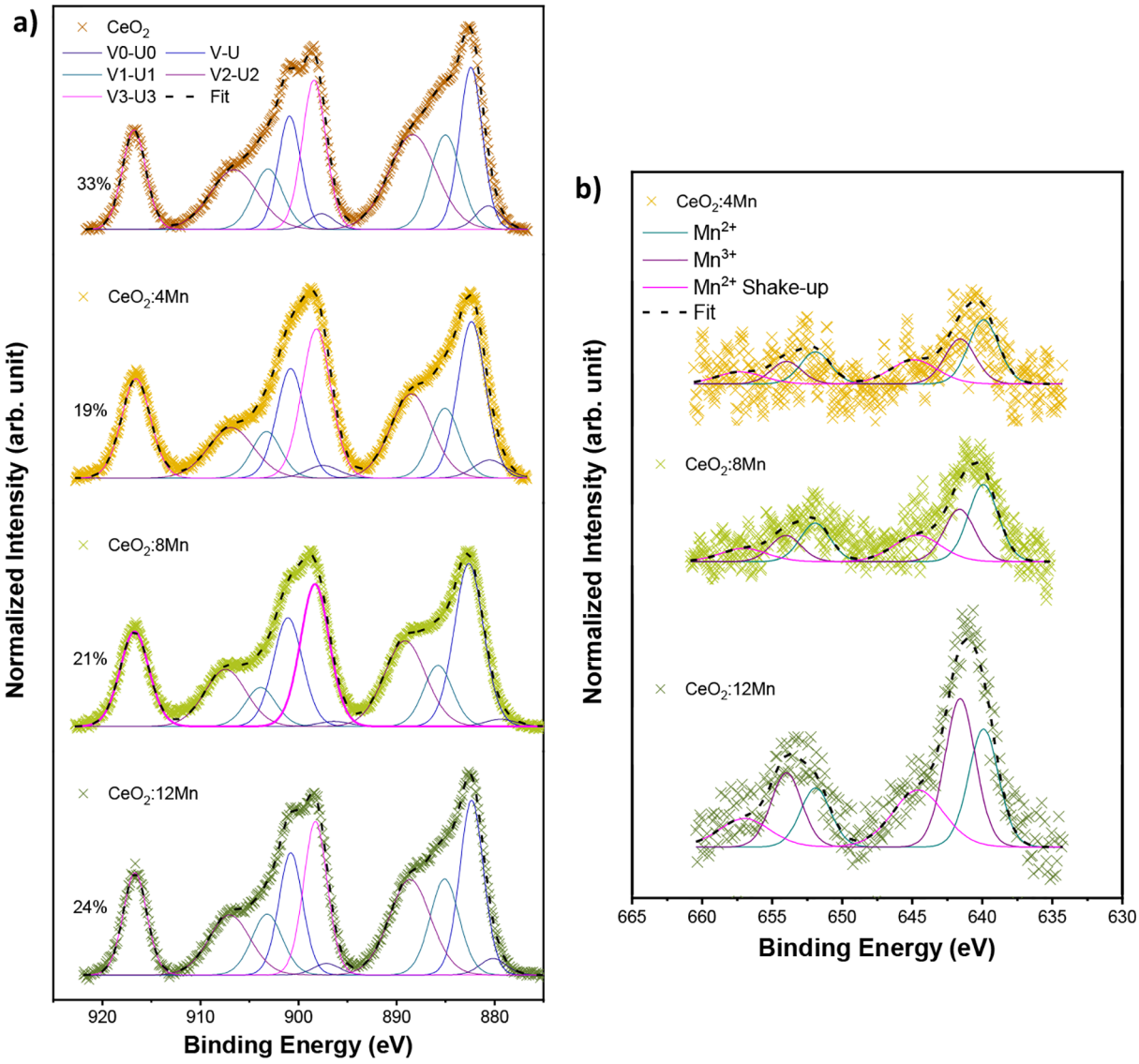

Figure 4. (A) XPS survey with the Ce^{3+} percentage and (B) Mn 2p spectra of the Mn-doped CeO_2 samples.

(iv), singly ionized (ii), and doubly ionized (iii) oxygen vacancies was also reported in the literature by many authors.[58−60]

Figure 3b illustrates the formation of clusters after the first introduction of the Mn^{2+} species $[MnO_4]^x$ into the CeO_2 lattice. The structure depicted in structure (i) can suffer from both electronic exchanges (ii) and the formation of structural defects (iv). The exchange between two electrons from an $[MnO_4]^x$ cluster and two different $[CeO_6]^x$ clusters results in the formation of an $[MnO_4]^{**}$ cluster containing Mn^{4+} species and two additional $[CeO_6]'$ clusters containing Ce^{3+} species (ii), while the output of an oxygen atom from the lattice generates a neutral oxygen vacancy $[V_o^x]$ (iv). Structure (iii), which contains an $[MnO_4]^*$ cluster with Mn^{3+} species, can be formed either when structure (ii) forms a singly ionized oxygen vacancy or after structure (iv) undergoes an electronic exchange between a neutral oxygen vacancy and an $[MnO_4]^x$ cluster and two different $[CeO_6]^x$ clusters, thus yielding a singly ionized oxygen vacancy $[V_o^{\bullet}]$, an $[MnO_4]^*$ cluster, and two $[CeO_6]'$ clusters. It is noteworthy that the $[MnO_4]^x$ cluster, which has five unpaired electrons, exhibits the strongest paramagnetic behavior. Considering that part of the Ce^{4+} species could be reduced to the Ce^{3+} configuration, this process likely stems from charges coming from Mn^{2+}, which in turn can generate Mn^{3+} and Mn^{4+},[61,62] reducing the amount of Mn^{2+} species.

When the Mn doping percentage increases, the electronic exchanges between the clusters change. Figure 3c shows the formation of clusters when the percentage of Mn in the lattice increases above 4 wt %. The structure, formed by $[MnO_4]^x$ and $[CeO_6]^x$ clusters containing Mn^{2+} and Ce^{4+} species, respectively, can undergo different electronic exchanges. The exchange between one electron from an $[MnO_4]^x$ cluster and a $[CeO_6]^x$ cluster leads to the formation of an $[MnO_4]^*$ cluster containing Mn^{3+} species and a $[CeO_6]'$ cluster containing Ce^{3+} (ii). The exchange between one electron from each of the two $[MnO_4]^x$ clusters and two different $[CeO_6]^x$ clusters generates two $[MnO_4]^*$ clusters containing Mn^{3+} species and two $[CeO_6]'$ clusters containing Ce^{3+} (iii). Finally, the exchange between two electrons from a $[MnO_4]^x$ cluster and two different $[CeO_6]^x$ clusters yields $[MnO_4]^{**}$ clusters containing Mn^{4+} species and two $[CeO_6]'$ clusters containing Ce^{3+} species

https://doi.org/10.1021/acs.inorgchem.3c01597
Inorg. Chem. 2023, 62, 12392−12402

(iv). Furthermore, structures (ii), (iii), and (iv) can be interconverted according to the electronic exchanges depicted in Figure 3c. Ceria has a small magnetic moment and, hence, a weak paramagnetic behavior. After the formation of a ceria-based solid solution with manganese, there is a strong increase in this paramagnetic feature, which is consistent with the formation of $[MnO_4]^x$ clusters containing Mn^{2+} species. However, as the amount of Mn increases, the formation of positively charged $[MnO_4]^*$ and $[MnO_4]^{**}$ clusters, which are less paramagnetic than the neutral $[MnO_4]^x$ clusters, is favored. Thus, the increase in the Mn content may cause a chaotic orientation of the magnetic dipoles, damaging the overall paramagnetic behavior, as reported by Al-Agel et al. and Hong et al.[63,64] This is in agreement with our experimental results because the integrated EPR signal does not increase linearly with the amount of Mn. Indeed, when the amount of Mn is doubled from 4 to 8 wt %, an only 20% increase in the integrated EPR signal is observed, while a further increment in the Mn content to 12 wt % results in a 35% increase.

XPS was used to characterize the surface states and compositions of the samples. Figure S1 displays the XPS survey spectra normalized with the Ce 3d maximum peak intensity, highlighting all of the observed transitions. The inset shows the XPS survey spectrum of the pure CeO_2 sample obtained with Mg Kα radiation and the expected overlap between the Ce LMM Auger and Mn 2p transitions. Usually, Mg Kα radiation is used in CeO_2-based samples because the Al source leads to an overlap between the Ce Auger electrons and the Ce 3d transitions. However, in this work, the Al source was mainly used because of the overlap between the Ce Auger electrons and the Mn 2p transitions, observed with the Mg source, severely affecting the Mn spectra due to the low signal-to-noise ratio. As expected, it is possible to visualize the elements Ce, O, Mn, and C, confirming the high purity of the samples.

According to the literature,[65] the Ce 3d spectra can be interpreted by assuming a model of five spin−orbit coupled doublets (Ce $3d_{5/2}$ and Ce $3d_{3/2}$): two for Ce^{3+} oxidation states and three for Ce^{4+} oxidation states (labeled in Figure 4a as V0−U0 and V1−U1 and as V−U, V2−U2, and V3−U3, respectively). These complex features have their origin in the hybridization of Ce 4f with O 2p binding orbitals and the partial occupation of the orbitals in the 4f valence state, giving rise to a well-known "shake-up" process, with some reports depicting 6−10 characteristic peaks.[66,67] In this way, our results confirm the presence of the Ce^{4+} and Ce^{3+} oxidation states in all studied samples. The amounts of Ce^{4+} and Ce^{3+}, corresponding to the $[CeO_8]$ and $[CeO_8{\cdot}V_o^i]$ clusters, respectively, can be correlated with the U3 peak derived from the transition between the $4f^0$ initial and final states. Because Ce^{3+} does not have this configuration, U3 becomes the fingerprint of the Ce^{4+} species. Assuming the occurrence of a uniform mixture of both oxidation states, the U3 peak intensity relative to the sum of all contributions to the Ce 3d region can be used to quantify the amount of Ce^{4+} (Ce^{3+}) present on the sample surface. Even though the XPS technique can overestimate the Ce^{3+}/Ce^{4+} ratio due to a possible photoreduction process,[68] a first decrease in the Ce^{3+} proportion from 33% to 19% can be seen when comparing the pure and the 4 wt %-doped samples, followed by a slight increase from 21% to 24% resulting from the already known metal promotion effect on ceria reduction.[69−71] The observed trend in the Ce^{3+} proportion was also corroborated by XPS analysis of the O 1s region shown in Figure S1.[72,73] In this sense, Aragón et al.[74] studied the influence of Fe doping on CeO_2 and observed, through XPS data, the coexistence of Ce^{3+} and Ce^{4+} ions as well as a decreasing tendency of the relative fraction of Ce^{3+} ions while increasing the iron content.

Figure 4b displays the Mn 2p spectra of the Mn-doped CeO_2 samples. As already mentioned, the low metal superficial concentration of these samples leads to a poor signal-to-noise ratio. Nevertheless, the obtained data evidence the typical spin−orbit coupled structure expected for Mn $2p_{3/2}$ and Mn $2p_{1/2}$. Going deeper into this analysis, we find that Mn can have several oxidation states from 0 to 8+, with some of them (i.e., Mn^{2+}−Mn^{4+} species) containing unpaired d electrons that spawn multiple-splitting XPS structures that (partially or totally) overlap, making it difficult to assign the correct species when these three oxidation states are present altogether.[75] In this context and on the basis of our EPR results, we propose a simplified three-spin−orbit coupled doublet model for the deconvolution of the Mn 2p region, which was tested with the CeO_2:12Mn sample and then propagated to the data obtained for the samples with less Mn. This model indicates that our XPS data are consistent with the presence of both Mn^{2+}, with the main peak and its characteristic "shake-up" structure being located at 640.0 and 644.6 eV, respectively, and Mn^{3+}, with the main peak appearing at 641.6 eV. However, the existence of Mn^{4+} cannot be ruled out due to the full signal overlap that occurs between them and Mn^{3+} species, corroborating the EPR data.

The atomic concentrations obtained from the deconvoluted spectra of the samples are summarized in Table 1. As observed,

Table 1. Surface Percentages of Atomic Concentrations from the Deconvoluted Spectra in Figure 4

sample	Ce^{3+} (%)	Ce^{3+} (%)	Mn^{2+} (%)	Mn^{3+} (%)
CeO_2	33	67	–	–
CeO_2:4Mn	19	81	58	42
CeO_2:8Mn	21	79	59	41
CeO_2:12Mn	24	76	44	56

the pure system has 33% of its cerium species in the Ce^{3+} configuration, which would lead to a complementary fraction of 67% Ce^{4+}. When the system is modified with 4 wt % Mn, there is an abrupt decrease in the amount of Ce^{3+} species to 19%, suggesting that 14% of the Ce^{3+} species are donating one electron to the Mn^{2+} ions entering the lattice, thus becoming nonparamagnetic Ce^{4+} species, which at first sight would indicate a reduction in the intensity of the EPR signal. On the contrary, 58% of the manganese species remain in the Mn^{2+} configuration with five unpaired electrons, justifying the paramagnetic feature of these samples. With an increase in the Mn content from 4 to 8 wt %, there is an increase in the amount of Ce^{3+} from 19% to 21%, while the amount of Mn^{2+} is kept virtually constant, increasing by only 1%, along with a decrease in the Mn^{3+} configuration from 42% to 41%. Upon modification of the content of Mn to 12 wt %, another increase in the amount of Ce^{3+} from 21% to 24% can be observed, together with a sudden decrease in the amount of Mn^{2+} from 59% to 44% and an increase in the Mn^{3+} configuration from 41% to 56%, which is EPR-silent. In this case, we can consider that the Mn^{2+} ions are donating one electron, becoming Mn^{3+}, but not to the Ce^{3+} species, because their concentration also increases. Thus, these charges are likely transferred to

https://doi.org/10.1021/acs.inorgchem.3c01597
Inorg. Chem. 2023, 62, 12392−12402

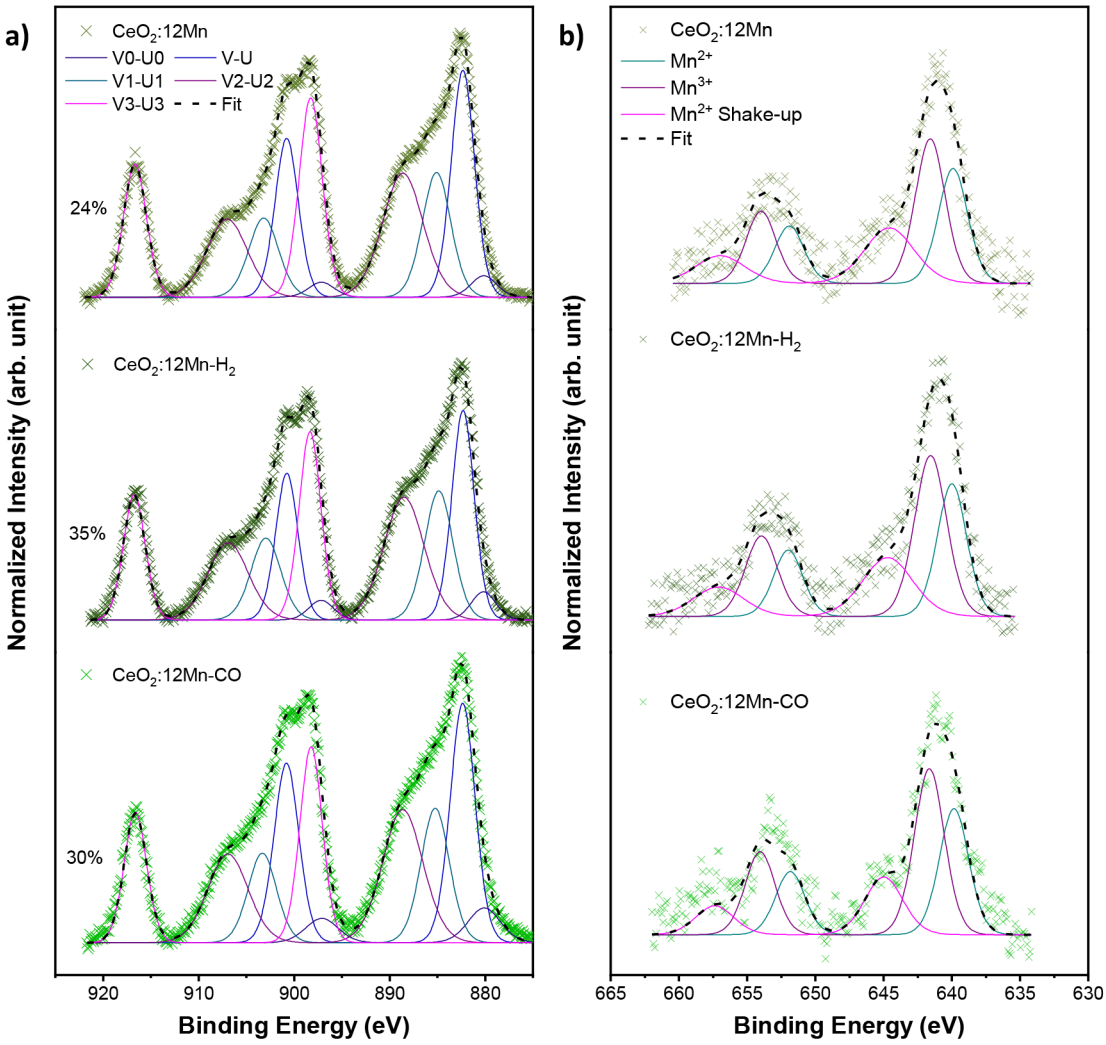

Figure 5. (A) Ce 3d and (B) Mn 2p XPS spectra for the treated samples.

neighboring defective neutral oxygen clusters, which then become singly ionized, enhancing the paramagnetic behavior of the sample.

To gain more insight into the surface species dynamics, the CeO_2:12Mn sample was analyzed after an *in situ* reduction treatment in a H_2 flow (70 mL/min) for 1 h at 400 °C and after an *ex situ* CO atmosphere treatment. It is known that the application of treatments with $H_{2(g)}$ and $CO_{(g)}$ to ceria can create V_o^i.[76,77] In this way, our aim was to understand the experimental mechanism responsible for the electronic exchanges between Ce^{3+} and Mn^{2+} species that generate the dipoles and quadrupoles seen in Figure 3, which can donate and receive electrons. Figure 5 shows the Ce 3d and Mn 2p spectra obtained for the treated samples. The untreated sample (CeO_2:12Mn) was also included as a reference. As observed, after reduction, the Ce^{3+} species increase from 24% to 35% due to the Mn promotion effect associated with V_o^i mobility.[78,79] Likewise, the Ce^{3+} concentration also increases to 30% after CO atmosphere treatment, in line with what was previously reported by Rocha et al. for La-doped CeO_2.[66] Accordingly, the levels of Mn^{2+} and Mn^{3+} are kept virtually constant under treatment in both atmospheres at 43% and 57%, respectively, compared to 44% and 56% for CeO_2:12Mn.

4. CONCLUSIONS

Mn-doped ceria nanostructures were obtained by using the MAH route after calcination at 500 °C, showing particle sizes of <40 nm. Raman and EPR analyses indicated the absence of Mn−O bonds and the presence of Mn-based defective clusters during interaction with CO. An increase in the number of paramagnetic species with an increase in the Mn content was observed. This was assigned to the presence of Mn^{2+} species resulting from the reduction of Mn^{3+} after interaction with CO. The association of Ce^{3+} and Mn^{2+} species with $V_o^{\bullet}$ seemed to be the most probable charge-compensating defect, because their number decreased along with particle size with an increase in Mn concentration. The XPS data confirmed the oxidation of some Mn^{2+} to Mn^{3+} and likely to Mn^{4+}, in addition to an increase in the number of Ce^{3+} species.

■ ASSOCIATED CONTENT

Supporting Information

The Supporting Information is available free of charge at https://pubs.acs.org/doi/10.1021/acs.inorgchem.3c01597.

XPS survey and O 1s high-resolution XPS spectra of the samples (PDF)

https://doi.org/10.1021/acs.inorgchem.3c01597
Inorg. Chem. 2023, 62, 12392−12402

AUTHOR INFORMATION

Corresponding Author

M. Assis − *Department of Analytical and Physical Chemistry, Jaume I University (UJI), Castelló 12071, Spain;* orcid.org/0000-0003-0355-5565; Email: marcelostassis@gmail.com

Authors

D. C. Amaral − *Advanced Materials Interdisciplinary Laboratory (LIMAV), Federal University of Itajubá (UNIFEI), Itabira 37500-903, Brazil*

L. S. R. Rocha − *Center for Research and Development of Functional Materials (CDMF), Federal University of São Carlos (UFSCar), São Carlos 13565-90, Brazil;* orcid.org/0000-0002-6059-2197

L. I. Granone − *Department of Chemistry and Biochemistry, FCEyN/IFIMAR, CONICET, National University of Mar del Plata, Mar del Plata B7606FWV, Argentina*

M. M. Lage − *Advanced Materials Interdisciplinary Laboratory (LIMAV), Federal University of Itajubá (UNIFEI), Itabira 37500-903, Brazil;* orcid.org/0000-0001-8591-2532

M. S. Churio − *Department of Chemistry and Biochemistry, FCEyN/IFIMAR, CONICET, National University of Mar del Plata, Mar del Plata B7606FWV, Argentina;* orcid.org/0000-0003-1239-6367

M. D. Sanchez − *Instituto de Física del Sur (IFISUR), Departamento de Física, Universidad Nacional del Sur (UNS), CONICET, Bahía Blanca B8000CPB, Argentina*

E. Longo − *Center for Research and Development of Functional Materials (CDMF), Federal University of São Carlos (UFSCar), São Carlos 13565-90, Brazil;* orcid.org/0000-0001-8062-7791

H. M. S. Nascimento − *Advanced Materials Interdisciplinary Laboratory (LIMAV), Federal University of Itajubá (UNIFEI), Itabira 37500-903, Brazil*

F. Moura − *Advanced Materials Interdisciplinary Laboratory (LIMAV), Federal University of Itajubá (UNIFEI), Itabira 37500-903, Brazil*

M. A. Ponce − *Advanced Materials Interdisciplinary Laboratory (LIMAV), Federal University of Itajubá (UNIFEI), Itabira 37500-903, Brazil; Physics and Engineering Research Center, National University of the Center of the Province of Buenos Aires (UNCPBA-CICPBA-CONICET), Tandil B7000GHG, Argentina; Institute of Materials Science and Technology (INTEMA), University of Mar del Plata (UNMdP), CONICET, Mar del Plata B7606 FWV, Argentina*

Complete contact information is available at: https://pubs.acs.org/10.1021/acs.inorgchem.3c01597

Notes

The authors declare no competing financial interest.

ACKNOWLEDGMENTS

The authors thank the following Brazilian agencies for their financial support: the Minas Gerais State Research Foundation (FAPEMIG), the National Council for Scientific and Technological Development (CNPq), and the São Paulo Research Foundation (FAPESP) [Grants 13/07296-2 (CEPID), 2018/20590-0 (PD), and 2020/02352-5 (BEPE)]. The authors also acknowledge the funding from the Agencia Nacional de Promoción Científica y Tecnológica, Argentina (PICT 2015-1832), and the Consejo Nacional de Investigaciones Científicas y Técnicas, Argentina (PUE 22920200100016CO-IFIMAR). M.A. was supported by Margarita Salas Postdoctoral Contract MGS/2021/21 (UP2021-021) financed by the European Union-Next Generation EU.

REFERENCES

(1) Acharya, S.; Bandyopadhyay, A.; Modak, S.; Mukherjee, S.; Das, D.; Chakrabarti, P. K. XRD, HRTEM, magnetic and Mössbauer studies on chemically prepared Fe3+-doped nanoparticles of cerium oxide. *J. Magn. Magn. Mater.* **2009**, *321*, 2701−2706.

(2) Lipp, M. J.; Jeffries, J. R.; Cynn, H.; Park Klepeis, J.-H.; Evans, W. J.; Mortensen, D. R.; Seidler, G. T.; Xiao, Y.; Chow, P. Comparison of the high-pressure behavior of the cerium oxides Ce2O3 and CeO2. *Phys. Rev. B* **2016**, *93*, No. 064106.

(3) Proetto, C.; López, A. Magnetic exchange interactions in cerium compounds. *Phys. Rev. B* **1982**, *25*, 7037−7039.

(4) Engelhardt, L. M.; Figgis, B. N. Magnetic susceptibility of cerium oxides. *J. Chem. Soc. A* **1969**, 2933−2937.

(5) Moreno, H.; Domingues, G. L.; Assis, M.; Ortega, P. P.; Mastelaro, V. R.; Ramirez, M. A.; Simões, A. Z. The Relationship between Photoluminescence Emissions and Photocatalytic Activity of CeO2 Nanocrystals. *Inorg. Chem.* **2023**, *62*, 4291−4303.

(6) Simonenko, T. L.; Simonenko, N. P.; Mokrushin, A. S.; Simonenko, E. P.; Glumov, O. V.; Mel'nikova, N. A.; Murin, I. V.; Kalinina, M. V.; Shilova, O. A.; Sevastyanov, V. G.; Kuznetsov, N. T. Microstructural, electrophysical and gas-sensing properties of CeO2−Y2O3 thin films obtained by the sol-gel process. *Ceram. Int.* **2020**, *46*, 121−131.

(7) Tian, D.; Li, K.; Wei, Y.; Zhu, X.; Zeng, C.; Cheng, X.; Zheng, Y.; Wang, H. DFT insights into oxygen vacancy formation and CH4 activation over CeO2 surfaces modified by transition metals (Fe, Co and Ni). *Phys. Chem. Chem. Phys.* **2018**, *20*, 11912−11929.

(8) Brant, A. T.; Giles, N. C.; Yang, S.; Sarker, M. A. R.; Watauchi, S.; Nagao, M.; Tanaka, I.; Tryk, D. A.; Manivannan, A.; Halliburton, L. E. Ground state of the singly ionized oxygen vacancy in rutile TiO2. *J. Appl. Phys.* **2013**, *114*, 113702.

(9) Montini, T.; Melchionna, M.; Monai, M.; Fornasiero, P. Fundamentals and Catalytic Applications of CeO2-Based Materials. *Chem. Rev.* **2016**, *116*, 5987−6041.

(10) Pîslaru-Dănescu, L.; Telipan, G.; Ion, I.; Marinescu, V. *Prototyping a Gas Sensors Using CeO_2 as a Matrix or Dopant in Oxide Semiconductor Systems*; Khan, S. B.; Akhtar, K., Eds.; Cerium Oxide; IntechOpen: Rijeka, Croatia, 2018; Chapter 5.

(11) Qi, J.; Zhao, K.; Li, G.; Gao, Y.; Zhao, H.; Yu, R.; Tang, Z. Multi-shelled CeO2 hollow microspheres as superior photocatalysts for water oxidation. *Nanoscale* **2014**, *6*, 4072−4077.

(12) Aboud, A. A.; Al-Kelesh, H.; El Rouby, W. M. A.; Farghali, A. A.; Hamdedein, A.; Khedr, M. H. CO_2 responses based on pure and doped CeO2 nano-pellets. *J. Mater. Res. Technol.* **2018**, *7*, 14−20.

(13) Simonenko, T. L.; Kalinina, M. V.; Simonenko, N. P.; Simonenko, E. P.; Glumov, O. V.; Mel'nikova, N. A.; Murin, I. V.; Shichalin, O. O.; Papynov, E. K.; Shilova, O. A.; Sevastyanov, V. G.; Kuznetsov, N. T. Synthesis of BaCe0.9-xZrxY0.1O3-δ nanopowders and the study of proton conductors fabricated on their basis by low-temperature spark plasma sintering. *Int. J. Hydrogen Energy* **2019**, *44*, 20345−20354.

(14) Gopal, C. B.; van de Walle, A. Ab initio thermodynamics of intrinsic oxygen vacancies in ceria. *Phys. Rev. B* **2012**, *86*, No. 134117.

(15) Huang, B.; Gillen, R.; Robertson, J. Study of CeO2 and Its Native Defects by Density Functional Theory with Repulsive Potential. *J. Phys. Chem. C* **2014**, *118*, 24248−24256.

(16) Ali, A.; Raza, R.; Khalil, R. M. A.; Ahmad, M. A.; Rafique, A.; Ullah, M. K.; Rehman, A ur; Mushtaq, M. N.; Belova, L. M. A potential electrolyte (Ce1-x CaxO2-δ) for fuel cells:Theoretical and experimental study. *Ceram. Int.* **2018**, *44*, 12676−12683.

(17) Simonenko, T. L.; Kalinina, M. V.; Simonenko, N. P.; Simonenko, E. P.; Glumov, O. V.; Mel'nikova, N. A.; Murin, I. V.; Shichalin, O. O.; Papynov, E. K.; Shilova, O. A. Spark plasma sintering of nanopowders in the CeO2-Y2O3 system as a promising approach to the creation of nanocrystalline intermediate-temperature solid electrolytes. *Ceram. Int.* **2018**, *44*, 19879−19884.
(18) Fernandes Vaz, I. C.; Tolentino Cabral, A. C.; Silva Procópio, A. M.; Moura Filho, F. Films based on cerium oxide sensitive to carbon monoxide. *Mater. Lett.* **2022**, *308*, No. 131174.
(19) Pradhan, N. Mn-Doped Semiconductor Nanocrystals: 25 Years and Beyond. *J. Phys. Chem. Lett.* **2019**, *10*, 2574−2577.
(20) Dismukes, G. C.; Sheats, J. E.; Smegal, J. A. Mn2+/Mn3+ and Mn3+/Mn4+ mixed valence binuclear manganese complexes of biological interest. *J. Am. Chem. Soc.* **1987**, *109*, 7202−7203.
(21) Xiao, M.; Zhang, X.; Yang, Y.; Cui, X.; Chen, T.; Wang, Y. M (M = Mn, Co, Cu)-CeO2 catalysts to enhance their CO catalytic oxidation at a low temperature: Synergistic effects of the interaction between Ce3+-Mx+-Ce4+ and the oxygen vacancy defects. *Fuel* **2022**, *323*, No. 124379.
(22) El-Achari, T.; Goumrhar, F.; Drissi, L. B.; Laamara, R. A. Structural, electronic and magnetic properties of Mn doped CeO2: An ab-initio study. *Physica B: Condensed Matter* **2021**, *601*, No. 412443.
(23) Yu, X.; Wu, X.; Chen, Z.; Huang, Z.; Jing, G. Oxygen vacancy defect engineering in Mn-doped CeO2 nanostructures for nitrogen oxides emission abatement. *Molecular Catalysis* **2019**, *476*, No. 110512.
(24) Qi, G.; Yang, R. T. Characterization and FTIR Studies of MnOx−CeO2 Catalyst for Low-Temperature Selective Catalytic Reduction of NO with NH3. *J. Phys. Chem. B* **2004**, *108*, 15738−15747.
(25) Zimou, J.; Nouneh, K.; Hsissou, R.; El-Habib, A.; Gana, L. E.; Talbi, A.; Beraich, M.; Lotfi, N.; Addou, M. Structural, morphological, optical, and electrochemical properties of Co-doped CeO2 thin films. *Materials Science in Semiconductor Processing* **2021**, *135*, No. 106049.
(26) Murugan, R.; Vijayaprasath, G.; Mahalingam, T.; Ravi, G. Defect induced magnetic transition in Co doped CeO2 sputtered thin films. *Ceram. Int.* **2016**, *42*, 11724−11731.
(27) Schilling, C.; Hofmann, A.; Hess, C.; Ganduglia-Pirovano, M. V. Raman Spectra of Polycrystalline CeO2: A Density Functional Theory Study. *J. Phys. Chem. C* **2017**, *121*, 20834−20849.
(28) Tuller, H. L.; Nowick, A. S. Small polaron electron transport in reduced CeO2 single crystals. *J. Phys. Chem. Solids* **1977**, *38*, 859−867.
(29) Yamazoe, N.; Fuchigami, J.; Kishikawa, M.; Seiyama, T. Interactions of tin oxide surface with O2, H2O AND H2. *Surf. Sci.* **1979**, *86*, 335−344.
(30) Batzill, M.; Diebold, U. The surface and materials science of tin oxide. *Prog. Surf. Sci.* **2005**, *79*, 47−154.
(31) Phokha, S.; Pinitsoontorn, S.; Chirawatkul, P.; Poo-arporn, Y.; Maensiri, S. Synthesis, characterization, and magnetic properties of monodisperse CeO2 nanospheres prepared by PVP-assisted hydrothermal method. *Nanoscale Res. Lett.* **2012**, *7*, 425.
(32) Kosacki, I.; Suzuki, T.; Anderson, H. U.; Colomban, P. Raman scattering and lattice defects in nanocrystalline CeO2 thin films. *Solid State Ionics* **2002**, *149*, 99−105.
(33) Weber, W. H.; Hass, K. C.; McBride, J. R. Raman study of CeO2: Second-order scattering, lattice dynamics, and particle-size effects. *Phys. Rev. B* **1993**, *48*, 178−185.
(34) Korepanov, V. I.; Hamaguchi, H. Quantum-chemical perspective of nanoscale Raman spectroscopy with the three-dimensional phonon confinement model. *J. Raman Spectrosc.* **2017**, *48*, 842−846.
(35) Zhang, X.; Qiao, X.-F.; Shi, W.; Wu, J.-B.; Jiang, D.-S.; Tan, P.-H. Phonon and Raman scattering of two-dimensional transition metal dichalcogenides from monolayer, multilayer to bulk material. *Chem. Soc. Rev.* **2015**, *44*, 2757−2785.
(36) Yang, S.; Zhang, Y. Spectroscopic ellipsometry study of Mn doped CeO2 thin films prepared by radio-frequency magnetron sputtering. *Thin Solid Films* **2022**, *760*, No. 139516.
(37) Conceição, E. J. F.; Aragón, F. F. H.; Urian, Y. A.; Castro, T. J.; Coaquira, J. A. H.; Morais, P. C.; da Silva, S. W. Effects of Gd doping on the structural, optical and magnetic properties of Ce1−xGdxO2−δ nanoparticles and the impact of the oxygen vacancy. *J. Alloys Compd.* **2023**, *960*, No. 170628.
(38) Endres, S. C.; Ciacchi, L. C.; Mädler, L. A review of contact force models between nanoparticles in agglomerates, aggregates, and films. *J. Aerosol Sci.* **2021**, *153*, No. 105719.
(39) Zhou, Y.; Ren, S.; Wang, M.; Yang, J.; Chen, Z.; Chen, L. Mn and Fe oxides co-effect on nanopolyhedron CeO2 catalyst for NH3-SCR of NO. *Journal of the Energy Institute* **2021**, *99*, 97−104.
(40) Chen, P.-L.; Chen, I.-W. Grain Growth in CeO2: Dopant Effects, Defect Mechanism, and Solute Drag. *J. Am. Ceram. Soc.* **1996**, *79*, 1793−1800.
(41) Mani Rahulan, K.; Angeline Little Flower, N.; Annie Sujatha, R.; Mohana Priya, P.; Gopalakrishnan, C. Third order nonlinear optical properties of Mn doped CeO2 nanostructures. *Optics & Laser Technology* **2018**, *101*, 358−362.
(42) Lee, K.-M.; Brito, M.; DeCoster, J.; Linskens, K.; Mehdi, K.; Lee, W.-I.; Kim, E.; Kim, H.; Kwon, G.; Nam, C.-Y.; Kim, T. Influence of oxidizing and reducing pretreatment on the catalytic performance of CeO2 for CO oxidation. *Molecular Catalysis* **2022**, *528*, No. 112465.
(43) Prohaska, J.; Trömel, M.; Rager, H. EPR study of Fe3+ and Mn2+ in CeO2 and ThO2. *Appl. Magn. Reson.* **1993**, *5*, 387−398.
(44) García Pintos, D.; Juan, A.; Irigoyen, B. Mn-Doped CeO2: DFT+U Study of a Catalyst for Oxidation Reactions. *J. Phys. Chem. C* **2013**, *117*, 18063−18073.
(45) Mansoor, H.; Harrigan, W. L.; Lehuta, K. A.; Kittilstved, K. R. Reversible Control of the Mn Oxidation State in SrTiO3 Bulk Powders. *Front. Chem.* **2019**, *7*, 353.
(46) Popov, A. L.; Popova, N. R.; Selezneva, I. I.; Akkizov, A. Y.; Ivanov, V. K. Cerium oxide nanoparticles stimulate proliferation of primary mouse embryonic fibroblasts in vitro. *Materials Science and Engineering: C* **2016**, *68*, 406−413.
(47) Dashdorj, J.; Zvanut, M. E.; Stanley, L. J. Iron-related defect levels in SrTiO3 measured by photoelectron paramagnetic resonance spectroscopy. *J. Appl. Phys.* **2010**, *107*, No. 083513.
(48) Kakazey, M.; Ivanova, N.; Boldurev, Y.; Ivanov, S.; Sokolsky, G.; Gonzalez-Rodriguez, J. G.; Vlasova, M. Electron paramagnetic resonance in MnO2 powders and comparative estimation of electric characteristics of power sources based on them in the MnO2−Zn system. *J. Power Sources* **2003**, *114*, 170−175.
(49) Hemantha Kumar, G. N.; Lakshmana Rao, J.; Gopal, N. O.; Narasimhulu, K. V.; Chakradhar, R. P. S.; Varada Rajulu, A. Spectroscopic investigations of Mn2+ ions doped polyvinylalcohol films. *Polymer* **2004**, *45*, 5407−5415.
(50) Rakhmatullin, R. M.; Semashko, V. V.; Korableva, S. L.; Kiiamov, A. G.; Rodionov, A. A.; Tschaggelar, R.; van Bokhoven, J. A.; Paun, C. EPR study of ceria nanoparticles containing different concentration of Ce3+ ions. *Mater. Chem. Phys.* **2018**, *219*, 251−257.
(51) Burbano, M.; Marrocchelli, D.; Yildiz, B.; Tuller, H. L.; Norberg, S. T.; Hull, S.; Madden, P. A.; Watson, G. W. A dipole polarizable potential for reduced and doped CeO2 obtained from first principles. *J. Phys.: Condens. Matter* **2011**, *23*, No. 255402.
(52) Gordon, R. A.; Haverkort, M. W.; Gupta, S. S.; Sawatzky, G. A. Orientation-dependent x-ray Raman scattering from cubic crystals: Natural linear dichroism in MnO and CeO2. *J. Phys.: Conf. Ser.* **2009**, *190*, No. 012047.
(53) Fuda, K.; Kishio, K.; Yamauchi, S.; Fueki, K.; Onoda, Y. 17 O NMR study of Y2O3-doped CeO2. *J. Phys. Chem. Solids* **1984**, *45*, 1253−1257.
(54) Vaz, I. C. F.; Macchi, C. E.; Somoza, A.; Rocha, L. S. R.; Longo, E.; Cabral, L.; da Silva, E. Z.; Simões, A. Z.; Zonta, G.; Malagù, C.; Desimone, P. M.; Ponce, M. A.; Moura, F. Electrical transport mechanisms of Neodymium-doped rare-earth semiconductors. *Journal of Materials Science: Materials in Electronics* **2022**, *33*, 11632−11649.

https://doi.org/10.1021/acs.inorgchem.3c01597
Inorg. Chem. 2023, 62, 12392−12402

(55) Esch, F.; Fabris, S.; Zhou, L.; Montini, T.; Africh, C.; Fornasiero, P.; Comelli, G.; Rosei, R. Electron localization determines defect formation on ceria substrates. *Science* **2005**, *309*, 752−755.
(56) Wang, L.; Yu, Y.; He, H.; Zhang, Y.; Qin, X.; Wang, B. Oxygen vacancy clusters essential for the catalytic activity of CeO2 nanocubes for o-xylene oxidation. *Sci. Rep.* **2017**, *7*, 12845.
(57) Thajudheen, T.; Dixon, A. G.; Gardonio, S.; Arčon, I.; Valant, M. Oxygen Vacancy-Related Cathodoluminescence Quenching and Polarons in CeO2. *J. Phys. Chem. C* **2020**, *124*, 19929−19936.
(58) Su, Z.; Yang, W.; Wang, C.; Xiong, S.; Cao, X.; Peng, Y.; Si, W.; Weng, Y.; Xue, M.; Li, J. Roles of Oxygen Vacancies in the Bulk and Surface of CeO2 for Toluene Catalytic Combustion. *Environ. Sci. Technol.* **2020**, *54*, 12684−12692.
(59) Das, T.; Nicholas, J. D.; Sheldon, B. W.; Qi, Y. Anisotropic chemical strain in cubic ceria due to oxygen-vacancy-induced elastic dipoles. *Phys. Chem. Chem. Phys.* **2018**, *20*, 15293−15299.
(60) Velu, S.; Shah, N.; Jyothi, T. M.; Sivasanker, S. Effect of manganese substitution on the physicochemical properties and catalytic toluene oxidation activities of Mg−Al layered double hydroxides. *Microporous Mesoporous Mater.* **1999**, *33*, 61−75.
(61) Saab, E.; Aouad, S.; Abi-Aad, E.; Zhilinskaya, E.; Aboukaïs, A. Carbon black oxidation in the presence of Al2O3, CeO2, and Mn oxide catalysts: An EPR study. *Catal. Today* **2007**, *119*, 286−290.
(62) Al-Agel, F. A.; Al-Arfaj, E.; Al-Ghamdi, A. A.; Losovyj, Y.; Bronstein, L. M.; Mahmoud, W. E. A novel recipe to improve the magnetic properties of Mn doped CeO2 as a room temperature ferromagnetic diluted metal oxide. *J. Magn. Magn. Mater.* **2014**, *360*, 73−79.
(63) Hong, W.-J.; Iwamoto, S.; Hosokawa, S.; Wada, K.; Kanai, H.; Inoue, M. Effect of Mn content on physical properties of CeOx−MnOy support and BaO−CeOx−MnOy catalysts for direct NO decomposition. *J. Catal.* **2011**, *277*, 208−216.
(64) Zhang, J.; Wong, H.; Yu, D.; Kakushima, K.; Iwai, H. X-ray photoelectron spectroscopy study of high-k CeO2/La2O3 stacked dielectrics. *AIP Advances* **2014**, *4*, 117117.
(65) Rocha, L. S. R.; Aparecido Ciola Amoresi, R.; Duarte, T. M.; Marana, N. L.; Sambrano, J. R.; Aldao, C. M.; Simões, A. Z.; Ponce, M. A.; Longo, E. Experimental and theoretical interpretation of the order/disorder clusters in CeO2:La. *Appl. Surf. Sci.* **2020**, *510*, No. 145216.
(66) Bêche, E.; Charvin, P.; Perarnau, D.; Abanades, S.; Flamant, G. Ce 3d XPS investigation of cerium oxides and mixed cerium oxide (CexTiyOz). *Surf. Interface Anal.* **2008**, *40*, 264−267.
(67) Cardenas, L.; Molinet-Chinaglia, C.; Loridant, S. Unraveling Ce3+ detection at the surface of ceria nanopowders by UPS analysis. *Phys. Chem. Chem. Phys.* **2022**, *24*, 22815−22822.
(68) Cong, Q.; Chen, L.; Wang, X.; Ma, H.; Zhao, J.; Li, S.; Hou, Y.; Li, W. Promotional effect of nitrogen-doping on a ceria unary oxide catalyst with rich oxygen vacancies for selective catalytic reduction of NO with NH3. *Chemical Engineering Journal* **2020**, *379*, No. 122302.
(69) Clark, A. H.; Marchbank, H. R.; Thompsett, D.; Fisher, J. M.; Longo, A.; Beyer, K. A.; Hyde, T. I.; Sankar, G. On the effect of metal loading on the reducibility and redox chemistry of ceria supported Pd catalysts. *Phys. Chem. Chem. Phys.* **2022**, *24*, 2387−2395.
(70) Acerbi, N.; Golunski, S.; Tsang, S. C.; Daly, H.; Hardacre, C.; Smith, R.; Collier, P. Promotion of Ceria Catalysts by Precious Metals: Changes in Nature of the Interaction under Reducing and Oxidizing Conditions. *J. Phys. Chem. C* **2012**, *116*, 13569−13583.
(71) Della Mea, G. B.; Matte, L. P.; Thill, A. S.; Lobato, F. O.; Benvenutti, E. V.; Arenas, L. T.; Jürgensen, A.; Hergenröder, R.; Poletto, F.; Bernardi, F. Tuning the oxygen vacancy population of cerium oxide (CeO2−x, 0. *Appl. Surf. Sci.* **2017**, *422*, 1102−1112.
(72) Soni, S.; Vats, V. S.; Kumar, S.; Dalela, B.; Mishra, M.; Meena, R. S.; Gupta, G.; Alvi, P. A.; Dalela, S. Structural, optical and magnetic properties of Fe-doped CeO2 samples probed using X-ray photoelectron spectroscopy. *Journal of Materials Science: Materials in Electronics* **2018**, *29*, 10141−10153.
(73) Aragón, F. F. H.; Aquino, J. C. R.; Ramos, J. E.; Coaquira, J. A. H.; Gonzalez, I.; Macedo, W. A. A.; da Silva, S. W.; Morais, P. C. Fe-doping effects on the structural, vibrational, magnetic, and electronic properties of ceria nanoparticles. *J. Appl. Phys.* **2017**, *122*, 204302.
(74) Biesinger, M. C.; Payne, B. P.; Grosvenor, A. P.; Lau, L. W. M.; Gerson, A. R.; Smart, R. St C. Resolving surface chemical states in XPS analysis of first row transition metals, oxides and hydroxides: Cr, Mn, Fe, Co and Ni. *Appl. Surf. Sci.* **2011**, *257*, 2717−2730.
(75) Li, Z.; Werner, K.; Chen, L.; Jia, A.; Qian, K.; Zhong, J.-Q.; You, R.; Wu, L.; Zhang, L.; Pan, H.; Wu, X.-P.; Gong, X.-Q.; Shaikhutdinov, S.; Huang, W.; Freund, H.-J. Interaction of Hydrogen with Ceria: Hydroxylation, Reduction, and Hydride Formation on the Surface and in the Bulk. *Chem. - Eur. J.* **2021**, *27*, 5268−5276.
(76) Jan, A.; Shin, J.; Ahn, J.; Yang, S.; Yoon, K. J.; Son, J.-W.; Kim, H.; Lee, J.-H.; Ji, H.-I. Promotion of Pt/CeO2 catalyst by hydrogen treatment for low-temperature CO oxidation. *RSC Adv.* **2019**, *9*, 27002−27012.
(77) Yang, M.; Shen, G.; Wang, Q.; Deng, K.; Liu, M.; Chen, Y.; Gong, Y.; Wang, Z. Roles of Oxygen Vacancies of CeO2 and Mn-Doped CeO2 with the Same Morphology in Benzene Catalytic Oxidation. *Molecules* **2021**, *26*, 6363.
(78) Liu, X.; Zhou, K.; Wang, L.; Wang, B.; Li, Y. Oxygen Vacancy Clusters Promoting Reducibility and Activity of Ceria Nanorods. *J. Am. Chem. Soc.* **2009**, *131*, 3140−3141.
(79) Liu, X.; Zhou, K.; Wang, L.; Wang, B.; Li, Y. Oxygen Vacancy Clusters Promoting Reducibility and Activity of Ceria Nanorods. *J. Am. Chem. Soc.* **2009**, *131*, 3140−3141.

https://doi.org/10.1021/acs.inorgchem.3c01597
Inorg. Chem. 2023, 62, 12392−12402